Sustainable Energy & Fuels

Interdisciplinary research for the development of sustainable energy technologies

Accepted Manuscript

This article can be cited before page numbers have been issued, to do this please use: L. Bottoni, H. Darjazi, L. Sbrascini, A. Staffolani, G. Pastore, L. Minnetti, F. Verdicchio, S. Gabrielli, A. Catorci and F. Nobili, *Sustainable Energy Fuels*, 2025, DOI: 10.1039/D5SE00645G.

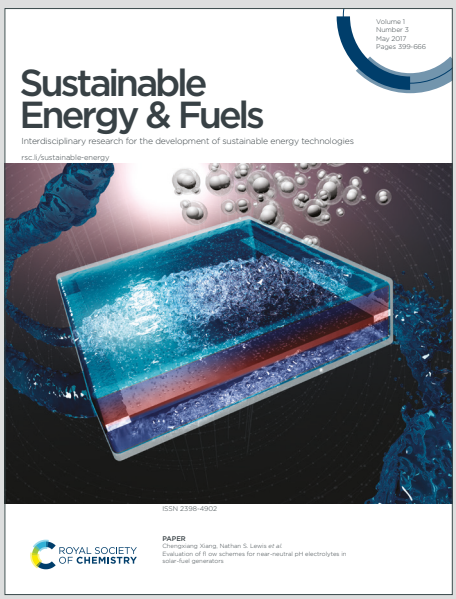

ROYAL SOCIETY OF CHEMISTRY

rsc.li/sustainable-energy

View Article Online
DOI: 10.1039/D5SE00645G

ARTICLE

A sustainable anode for Na-ion batteries based on holm oak waste-derived hard carbon and lignin binder

Received 00th January 20xx,
Accepted 00th January 20xx

DOI: 10.1039/x0xx00000x

Luca Bottoni,*[a] Hamideh Darjazi, [a,b,†] Leonardo Sbrascini,[a] Antunes Staffolani,[a,‡] Genny Pastore,[a] Luca Minnetti,[a,b] Federico Verdicchio,[a,b] Serena Gabrielli,[a] Andrea Catorci[c] and Francesco Nobili[a,b]

Sodium-ion batteries (SIBs) represent one of the key-enabling technology for the ongoing energy transition. However, the economic success of SIBs relies on sustainable and low-cost electrode materials such as the bio-derived ones. Particularly, it is important to find an environmentally friendly alternative to the commercial binder polyvinylidene fluoride, which currently poses several concerns, as for the other perfluorinated alkylated substances (PFAS), in terms of high environmental impact. In this context, a holm oak waste biomass was used both for the production of hard carbon and as a source of lignin, a natural binder currently poorly valorized. A one-step pyrolysis of holm-oak waste followed by acid leaching were performed to obtain a hard carbon with low amount of impurities, good interlayer spacing and well-developed microporosity and surface area. On the other hand, lignin has been extracted from holm oak waste feedstock through an organosolv process with a binary mixture of γ-valerolactone and water, obtaining a lignin with high level of purity. The obtained materials were combined to prepare a bio-based anode materials for SIBs, exhibiting around 200 mAh g^{-1} reversible capacity in Na half-cells cycled at 300 mA g^{-1}, with promising rate capability and long cycling stability even at high current rates. The electrochemical results combined with the interfacial and post-mortem SEM analysis demonstrated the ability of lignin binder to ensure longstanding adhesion with hard carbon substrate, reflecting into electrodes with long cycle life and capacity retention.

1. Introduction

Currently lithium-ion batteries (LIBs) represent the most used energy storage technology for a wide range of applications thanks to their relatively high energy (up to 260 Wh kg^{-1})[1] and power densities (600-3000 W kg^{-1}), high round-trip efficiency, long cycle life (500-10000 cycles) and low self-discharge (around 1-5 % per month).[2] However, the huge increases in LIBs demand, mainly driven by electrified vehicles market,[3] is posing serious concerns about the future availability of the European Union critical raw materials necessary for lithium-ion batteries, such as lithium, cobalt, nickel, natural graphite and fluorine.[4] In this context, sodium-ion batteries (SIBs) represent a promising alternative respect to LIBs, particularly appealing for large-scale stationary energy storage[5,6] mainly thanks to more than 1000-time higher abundance of Na resources than Li and wider global distribution,[7] which result in lower cost of Na-containing raw materials (0.19 $ kg^{-1} for Na_2CO_3 vs. 10.49 $ kg^{-1} for Li_2CO_3 in February 2025).[8] Other key advantages of SIBs are the lower reliance on critical raw materials such as those mentioned above and the possibility of use aluminum current collectors for both cathode and anode electrodes. This is beneficial for the decrease of cost and weight, and the possibility of storage at fully discharged state, making handling and transportation safer.[9]All these aspects coupled with sustainable manufacture processes concur in determining low costs and large opportunities for SIBs penetration into the LIBs market, especially that of stationary storage. Despite LIBs and SIBs share the same "rocking chair" working principle, there are some differences between these systems, which imply that materials used in LIBs cannot be transferred straightforward to the SIB counterpart. This is the case of graphite, the state-of-the-art anode material for LIBs, which exhibit poor performances in sodium-ion systems, mostly because of thermodynamic limitations for Na intercalation into graphite.[10] More interesting results have been obtained using non-graphitizable carbons, known as hard carbons (HCs), which are currently the "first-generation" active material at anode side for SIBs.[11] HCs are characterized by disordered and incoherent structures, resulting into a sodium storage mechanism which is not completely elucidated yet.[10,12] Nonetheless, they exhibit appealing properties as anodes, due to high storage capacity and low operating voltage (~ 0.1 vs Na^+/Na). HCs are generally synthesized from several carbon-rich precursors, both synthetic and natural, through a solid-phase pyrolysis in the temperature range 600-1500 °C.[13,14] Among the precursors, raw biomasses are the most explored feedstocks for HC production, being cheap, renewable and widely distributed.[15] In particular, lignocellulosic biomasses such as agricultural by-products

[a] School of Science and Technology, Chemistry Division, University of Camerino, Via Madonna delle Carceri snc, Camerino, Italy
[b] GISEL- Centro di Riferimento Nazionale per i Sistemi di Accumulo Elettrochimico di Energia, INSTM, Via Giuseppe Giusti 9, Firenze, Italy
[c] School of Biosciences and Veterinary Medicine, University of Camerino, Via Pontoni 5, Camerino, Italy
† Current Affiliation: Group of Applied Materials and Electrochemistry – GAME Lab, Department of Applied Science and Technology – DISAT, Politecnico di Torino, Corso Duca degli Abruzzi 24, Torino, Italy
‡ Current Affiliation: Department of Chemistry "Giacomo Ciamician", University of Bologna, Via Francesco Selmi 2, Bologna, Italy

and forestry residues represent the major waste biomass in the world: only Italy produces around 20 million tons per year of crop by-products and 2 million tons per year of forest residues.[16] In this context, the utilization of lignocellulosic waste for the production of value-added materials such as HCs is both beneficial for the sustainability of SIBs industry and also for the agroforestry waste management. However, if on the one side agricultural by-products are extensively evaluated as potential precursors for HCs production, on the other side forest residues are, to the best of our knowledge, less investigated, despite they share the same chemical composition of agricultural analogues, being composed of cellulose, hemicellulose and lignin as building blocks of plant cell walls.[17]

Another electrode key component is the binder material, which act as a glue between active material, conductive agent and current collector. Although it is generally present at low-percentages (2-5 %wt),[18] its binding ability and stability ensure prolonged physical and electrical contact within electrode components, improving the cycle life of the cell. An ideal binder should meet some important requirements. Among them, its environmentally friendly nature, low-cost and aqueous processability are becoming crucial properties. Polyvinylidene fluoride (PVDF), the state-of-the-art binder material for LIBs, have some important ecological limitations: firstly, it is dissolved in the toxic and expensive N-methyl-2-pyrrolidone (NMP);[19] secondly, PVDF belongs to the poly- and perfluoroalkylsubstances (PFAS), which are characterized by high environmental concerns due to their high persistence in ecosystems and bioaccumulation capability in living organisms.[20] In light of these concerns and to the recent actions put in place by authorities all over the world to limit the use of PFAS,[21] the research toward F-free and bio-based binder materials is currently a key research and development topic in battery industry. In this context, different bio-based binders have been proposed recently, among them, the sodium salt of carboxymethylcellulose (Na-CMC) is the most important alternative to PVDF and is gradually replacing it at anode side.[18] Lignin, the second most abundant biopolymer on Earth, could be another promising binder material for rechargeable batteries thanks to its chemical structure, being an heterogeneous aromatic polymer with an amorphous 3D network given by a high level of crosslinks and branches.[22] The aromatic skeleton mainly provides structural rigidity and thermal stability, the highly crosslinked structure can ensures robust adhesiveness through mechanical bonding, while the abundant polar functional groups can enable the formation of hydrogen bonds with active material and additives, enforcing the chemical binding ability.[23,24] Beyond technical aspects, lignin meets other important requirements such as renewability and large abundance worldwide, being a common by-product of pulp and paper industry. Globally, industry produces around 50 million tons per year of lignin, of which the 95 % is disposed or used as low-quality fuel while only the 5 % is reused for value-added applications.[25] Nonetheless, its application as binder material has not been much explored so far: to the best of our knowledge, few studies were done using lignin or its derivatives as binder in electrode materials for LIBs[25–28] and SIBs.[29] The main issue regarding the use of lignin as binder is related to its compatibility with active material substrate and common electrolyte solvents, which can result in poor adhesion and instability of electrode/electrolyte interface. Moreover, the exact molecular structure of lignin as well as some physical and chemical properties (i.e. molecular weight, solubility, thermal properties) depends on its origin and also on the extraction method. Therefore, huge efforts are required to assess the feasibility of using lignin as binder material for rechargeable batteries, especially focusing the attention into the electrochemical behavior and stability upon cycling. Among the extraction processes, the organosolv method has been considered as one of the most promising methods to isolate lignin for the production of biomaterials, since it allows to obtain high-quality lignin in terms of purity and sulphur-free nature. For the organosolv extraction, the conventional organic solvents are progressively replaced by novel biomass-derived solvents, such as γ-valerolactone (GVL). GVL is a bio-based, non-toxic and recyclable solvent which effectively promote delignification of biomass when it is coupled in binary system with water.[30,31] Herein, holm-oak waste (*Quercus Ilex*) has been used both as feedstocks for the synthesis of hard carbon and as a lignin source for the extraction by GVL:H_2O mixture. Then, the obtained materials are combined and used for the production of bio-based anode electrodes, which are tested to assess the feasibility of use of organsolv-extracted lignin as binder material with hard carbon substrate in Na half-cells.

2. Experimental

2.1 Synthesis of Holm Oak-Derived Hard Carbon

The holm oak waste was collected from the Alte Valli of Rivers Potenza and Chienti, a wooded area in Marche Apennines (Italy). The air-dried sample was sieved to particle size < 1 mm. Then the ground biomass was submitted to a preliminary water leaching to remove impurities. In details, the samples were put in deionized water (sample:water ratio 1:50) and heatead to 60 °C for 12 h under stirring. After that, the biomass was filtered, washed two times with fresh water and dried at 80° C overnight. Then the dried raw material was ground to a fine powder with an automated ball mill at 300 rpm for 4h in a steel jar (ball-to-powder ratio 1:50 in weight) and carbonized in a horizontal cylindrical furnace at 1000 °C for 2 h under nitrogen flow after a heating ramp of 5 °C min^{-1}. The sample was cooled down inside the furnace, under nitrogen flow as well, then submitted to an acid leaching in HCl 3M (sample:solution ratio 1:20) for 3 days under vigorous stirring at room temperature. Finally, the sample was filtered and washed with deionized water, until a neutral pH was obtained, and stored at 80° C overnight. The hard carbon obtained was labelled as LHC.

2.2 Extraction of Lignin

The extraction of lignin was performed by broadly performing an organosolv method reported elsewhere.[32] Briefly, the biomass was dried and milled to a particle size < 1 mm and suspended into a mixture GVL with H_2O in the ratio 1:1 w/w using a solid-to-solvent ratio 1:10 w:w. The resulting mixture was put into a microwave reactor and heated for 2h at 170 °C under vigorous stirring. Subsequently, the solution was cooled down below 50 °C. After that, the mixture was filtered and the solid residue was washed, dried and weighted to determine the pulp yield. The lignin contained in the filtrate ("organosolv liquor") was precipitated using fresh water and collected using centrifugation. The extracted lignin sample was dried in an oven overnight and labelled as LGN.

2.3 Electrode Processing and Cell Assembling

Anodes were made by using LHC as the active material, Super-P carbon (Imerys) as the conductive agent, and LGN as the binder. HC:Super-P:Lignin (80:10:10 w/w) slurries were dispersed in GVL, coated onto Al foil using the doctor blade technique (thickness of wet coating = 100 µm), and left to dry at room temperature. Same procedure has been followed for PVDF- and CMC-based electrodes except for the dispersion which has been conducted in N-methyl-2-pyrrolidone (NMP) and water, respectively. After calendaring, circular electrodes (9-mm diameter) were cut and further dried at 120 °C under vacuum for 12 h. The loadings of active materials were in the range 0.6-1.0 mg cm^{-2} for all the electrodes. Na half-cells were prepared by assembling three-electrode Swagelok-type cells in an argon-filled glove box (Jacomex GP-campus, oxygen and moisture content less than 0.8 ppm) using LHC-based anodes as working electrode and metallic sodium (Sigma-Aldrich) as reference and counter electrodes. A 1 M solution of $NaClO_4$ (Sigma-Aldrich) in ethylene carbonate (EC)/ propylene carbonate (PC) (1:1 in volume) (Sigma-Aldrich) was selected as the electrolyte (400 µl) and 12 mm glass fiber disks (Whatman GF/A) as separator.

2.4 Material Characterizations

The constituent analysis of oven-dried holm-oak feedstock was conducted following the NREL protocols TP-510-42619 "Determination of Extractives in Biomass"[33] and TP-510-42618 "Determination of Structural Carbohydrates and Lignin in Biomass".[34] Holocellulose content was estimated as difference between the sum of the other constituents and the total 100 % given by the oven dry weight sample. For the extracted lignin, the TP-510-42618 protocol was used to estimate the purity of lignin sample and the effectiveness of the extraction. All the determinations were repeated two times. Infrared spectra (FT-IR) of the LGN powder was recorded by means of a Perkin-Elmer Spectrum Two FTIR spectrometer within the wave number range of 400 to 4000 cm^{-1}. Thermogravimetric analysis (TGA) of LGN was carried out using a Perkin-Elmer STA 6000 Thermal Analyzer. The nitrogen flow rate at the powder was set to 50 mL min^{-1} and an alumina crucible was used to hold the sample. After equilibration, the powder was heated up to 800 °C at a rate of 10 °C min^{-1}. Gel Permeation Cromatography (GPC) was performed to determine the molecular weight of lignin binder. Agilent 1260 Infinity II Multi Detector Suite (MDS) was used for the analysis. The instrument is equipped with a guard column (Agilent GPC/SEC Guard Column) followed by two columns in series (PLgel MIXED-C and PLgel MIXED-D). Three different detectors are installed on the device: a dual light scattering detector (measuring in the angles of 15° and 90°), a refractive index detector and a viscosity detector. THF was used as mobile phase with a flow rate of 1.0 ml/ min. The standards used for column calibration were polystyrene standards with different M_p values in the range of 580–283800 g mol^{-1}. For the measurements and data analysis, an Agilent GPC/SEC Software was used. Prior the analysis, the lignin sample was acetylated using a mixture of glacial acetic acid:acetyl bromide (9:1 v/v) for 6h. Then the solvent mixture was removed under vacuum and the acetylated lignin was dissolved in THF (1 mg ml^{-1}). Scanning Electron Microscopy (SEM) and Energy Dispersive X ray analysis (EDX) of the hard carbon sample and electrodes were acquired using a FESEM Cambridge Stereo scan 360 electron microscope equipped with QUANTAX EDX detector (at an accelerating voltage of 15 kV). The cycled electrode was washed with dimethyl carbonate before submitting to *post-mortem* analysis. The structure of the hard carbon powder was characterized by X-ray diffraction (XRD) (Bragg–Brentano geometry, Cu-Kα, λ = 1.54059Å) and Raman spectroscopy (Horiba IHR 320, wavelength 532 nm). The interplanar spacing (d_{002}) was calculated according to the Bragg's Law (eqn (1)):

$$d_{002} = \lambda \,/\, 2sin\,(\theta_{002}) \quad (1)$$

with λ = 0.154 nm. The crystallite size along c-axis (staked plane height) L_c was estimated according to the Scherrer's Equation (eqn (2)):

$$\mathrm{L}_c = \mathrm{K}\lambda \,/\, \beta_{002}\cos(\theta_{002}) \quad (2)$$

where K is a shape factor which corresponds to 0.9 and β is the full width at half maximum of (002) peak.[35] Moreover, the average width of graphene domain L_a was also estimated using Raman technique according to the eqn (3):

$$L_a = (2.4\mathrm{E}^{-10})\,\lambda^4\,(I_\mathrm{G}\,/I_\mathrm{D}) \quad (3)$$

Pore characteristics of holm-oak derived HC was evaluated by CO_2 adsorption measurement at 273 K using a Micromeritics ASAP 2020 instrument. Prior the adsorption, the sample has been outgassed for 12 h at 150 °C. The specific surface area was calculated by the BET model while the Pore Size Distribution (PSD) was calculated according to the DFT method.

2.5 Electrochemical Characterizations

All electrochemical tests were carried out using a VMP-2Z multichannel electrochemical workstation by Bio-Logic Science Instruments (France). Cyclic voltammetry of holm-oak derived HCs electrodes in Na half-cell were performed at different scanning rate ranging from 0.10 mV s^{-1} and 1.00 mV s^{-1} in the voltage range 0.01 to 2 V vs Na^+/Na. Galvanostatic charge/discharge and rate capability tests of the hard carbon electrodes in Na half-cells were collected with the voltage ranging between 0.01 and 2 V, assuming for all the experiments that 1C rate corresponds to 300 mA g^{-1} with respect to active material mass. In addition, C-rate capability of the LHC electrodes were evaluated in the C/5 to 5C range (5 cycles at every rate). In order to evaluate the interfacial behavior of electrodes, electrochemical impedance spectroscopy (EIS) was carried out at the first cycle and then at each tenth cycle at E_{we} = 0.4 V, with an AC amplitude of 5 mV, in a frequency range 100 kHz > *f* > 10 mHz.

3. Results and discussion

3.1 Chemical, Structural and Morphological Characterizations of the Holm Oak-Derived Hard Carbon

The yield % of holm oak pyrolysis to produce hard carbon was calculated to be 22.4 % (hard carbon/biomass precursor ratio).

However, this value comprises also the residual ashes coming from biomass precursor. Therefore, to estimate the amount of inorganic impurities, EDX analysis was performed on the hard carbon powder obtained by the pyrolysis. The results, shown in

Figure **1**a, reveal, in addition to carbon and oxygen, the presence of heteroelements such as sulphur, chlorine and especially calcium, accounting for a total atomic percentage of around 1.9 at. % in the untreated hard carbon powder. However, since the inorganic impurities strongly affect the structural, textural and electrochemical properties of hard carbons,[36] acid leaching was performed on holm oak-derived hard carbon powder and the effectiveness of the leaching to remove the inorganic fraction was evaluated trough EDX analysis of the hard carbon obtained after leaching and neutralization. As shown in

Figure **1**b and Table 1, the atomic percentage of carbon increases from around 88 at. % to 96 at. %, as a consequence of the decrease of both oxygen and calcium contents. This trend suggests that Ca-containing inorganic impurities such as oxides and/or carbonates are dissolved in HCl and removed during the filtration. A sensible increase in the Cl atomic percentage was detected due to the residual chlorine after hydrochloric acid leaching. Overall, the sum of atomic percentage of heteroelements decreases from 1.91 % to 0.58 at. %. The removal of these inorganic compounds might be beneficial for the electrochemical performance, since they may otherwise occupy available active sites for Na uptake, as well as decrease the electronic conductivity or affect the electrode surface chemistry.[37] For the sake of clarity, the intensity of Cl and Ca peaks seems to be much higher than that of O in EPMA spectra (

Figure **1** a,b), thus indicating a much higher amount of these heteroelements respect to O. It should be noted that, in the absence of a flat and highly polished surface standard, a proper quantification of O cannot be performed: lighter elements (i.e., O and C) generally yield low-energy photons that are susceptible to self-absorption when an energy beam E_0 > 3 keV is employed for the measurement. This phenomenon can lead to a lowering of the intensity of the O peak with respect to other heavier elements, thus underestimating the amount of O when considering relative intensities.[38] In order to deeply evaluate the effectiveness of acid leaching to remove ash, XRD analysis were performed before and after acid leaching, as shown in

Figure **1** c,d. The peaks marked with the * present both in non-leached and acid-leached samples belong to the brass sample holder. On the other hand, the peaks of hard carbon are located at ~ 22-23° and 43°, which can be assigned to the (002) and (100) crystallographic planes,[39] while the presence of impurities is indicated by sharp peaks clearly visible for no-acid treated material, thus evidencing the effectiveness of acid leaching to remove them. Therefore, structural, morphological and electrochemical characterizations were performed only on acid-leached hard carbon, which will be mentioned only as LHC.

Regarding the above-mentioned characteristic peaks of hard carbon, the (002) band indicates the spacing between graphene layers and the broadening of the signal is consistent with the presence of short-range structures composed of a random layer lattice with defective sites and crystalline graphitic domains.[40,41] Generally, the synthetic conditions play a primary role in determining the d_{002} of hard carbon respect to the biomass composition, although the presence of high ash content in the feedstock is thought to prevent reorganization of carbon atoms and thus graphitization.[42] The d_{002} of LHC sample has been calculated, according to the Bragg's Law reported in eqn (1), as 0.392 nm, in line with other hard carbon found in the literature.[37,43] This value is higher than that of graphite (0.33 nm) and soft carbon (~ 0.35 nm), thus facilitating the sodium insertion/de-insertion into hard carbon. (~ 0.35 nm), thus facilitating the sodium insertion/de-insertion into hard carbon.

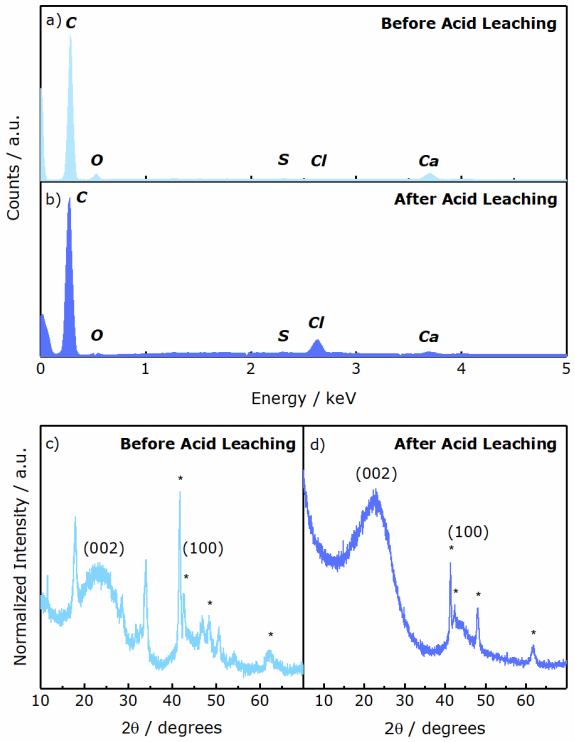

Figure 1 EDX analysis of holm oak-derived HC (a) before and (b) after acid-leaching; XRD spectra of holm oak-derived HC (c) before and (d) after acid-leaching.

Table 1 Atomic percentage of elements estimated from EDX analysis of holm oak-derived HC before and after acid-leaching.

Sample	Element (at. %)				
LHC	**C**	**O**	**S**	**Cl**	**Ca**
Before Acid Leaching	88.50	9.60	0.07	0.07	1.77
After Acid Leaching	96.84	2.58	0.03	0.46	0.09

Regarding the other lattice parameters, the stacked plane height L_c is 0.760 nm, while the number of interlayers stacked in the graphitic domains *n*, estimated according to the calculation $n = L_c/d_{002} + 1$, reveals approximatively 3-4 stacked graphene layers in the graphitic domains for LHC.[44] Additional information about materials were obtained using Raman Spectroscopy on LHC powders. As shown in Figure 2a, the two typical bands of layered carbon are located at around 1336 cm^{-1} (D-band) and

View Article Online
DOI: 10.1039/D5SE00645G

ARTICLE

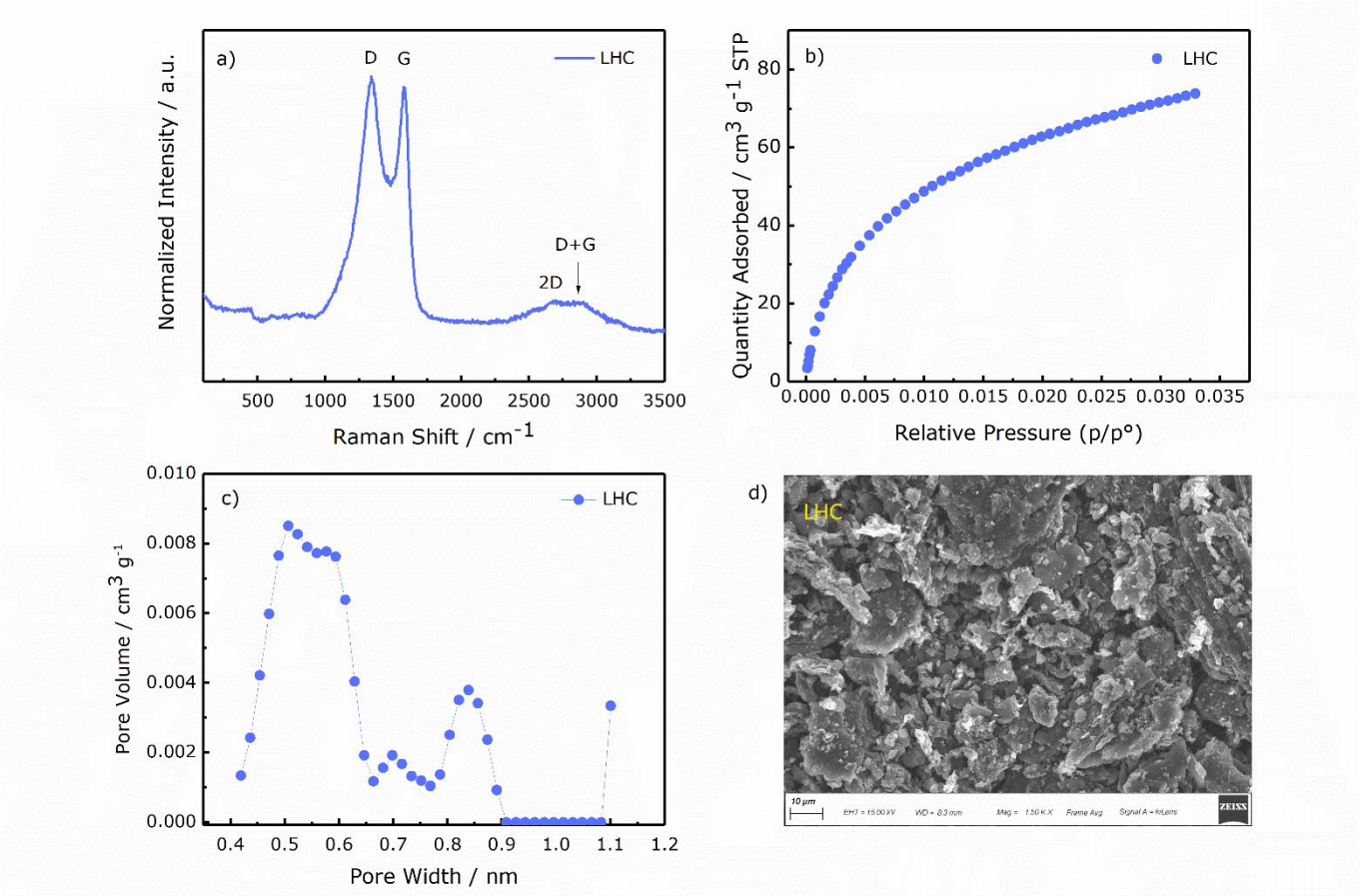

Figure 2 Chemical and morphological characterizations of LHC powder: (a) Raman spectra; (b) CO_2 adsorption-desorption isotherm; (c) Pore Size Distribution (d) SEM image. Magnification: 1500 x.

Table 2 LHC structural and physical properties.

d_{002} (nm)	L_c (nm)	L_a (nm)	I_G/I_D	*n*	SSA CO_2 (m^2 g^{-1})
0.392	0.760	18.46	0.960	3.49	320.3

1580 cm^{-1} (G-band). Moreover, two broad and low intensity peaks are located at ~ 2680 cm^{-1} and 2880 cm^{-1}, which correspond to the second-order bands 2D and D+G, respectively. From the intensity ratio between the G band and the D band (I_G/I_D), the degree of graphitization of LHC is calculated to be 0.96, in line with other hard carbons synthesized at similar annealing temperature.[45] Although the D band generally reflects the presence of disorder and defects in the sp^2 network of carbon materials, it has been found that for hard carbon with crystallite size L_c below 2.0 nm such as LHC, the presence of a predominant D band can be correlated with a high level of structural order and limited defect density.[14] From the eqn (3), the average width of the graphitic domains L_a is calculated to be 18.46 nm. To investigate the hard carbon properties, CO_2 adsorption measurement was performed. The obtained isotherm is shown in Figure 2b while the calculated DFT pore size distribution is shown in Figure 2c. The value of CO_2 BET specific surface area (SSA) is calculated to be 320.3 m^2 g^{-1}: this relatively large SSA is expected to promote considerable electrolyte decomposition during the first sodiation, decreasing

the initial coulombic efficiency % (ICE) of the hard carbon. However, since CO_2 is able to detect also the narrowest micropores, their presence in the sample "apparently" increases the calculated SSA with respect to the common SSA values obtained with N_2, which is not able to access them. Indeed, the DFT pore size distribution confirms presence of a certain moiety of micropores, with most of the micropores having size described by a gaussian-type curve in the range 0.4 - 0.7 nm, representing around the 78 % of the total volume created by micropores with size ≤ 1.1. These so-called "ultramicropores" are involved in the Na^+ storage, providing extra sites for sodium adsorption.[46] Finally, the SEM image (Figure 2d) of LHC powder reveals an irregular particle size distribution in the micrometer range with a flake-like morphology. All the structural parameters of the acid leached LHC powder are summarized in Table 2.

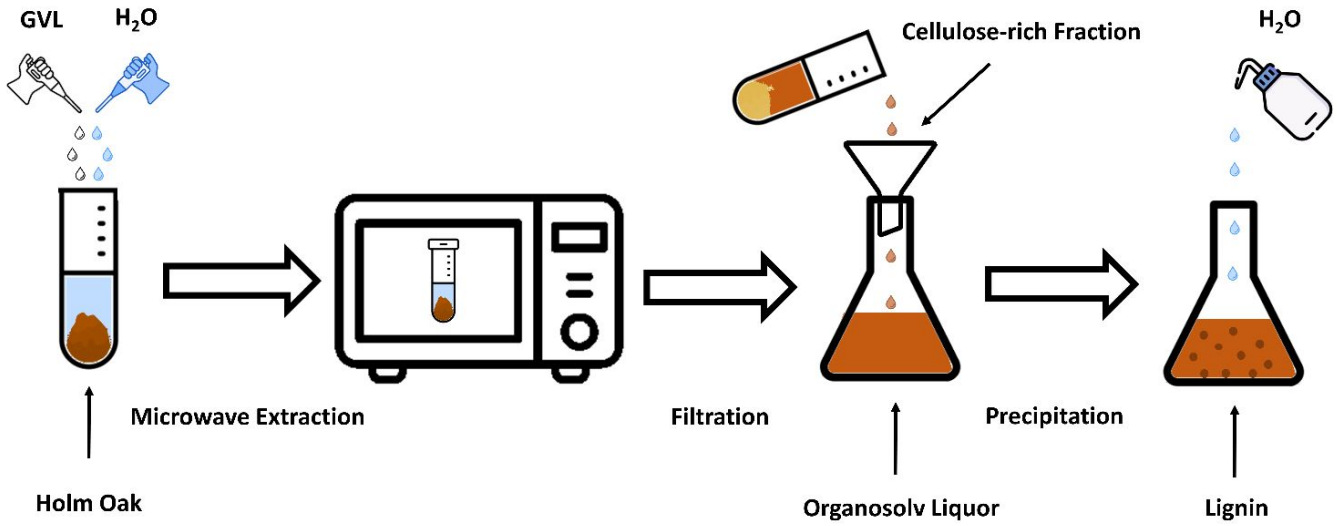

Figure 3 Schematic representation of lignin extraction

3.2 Extraction, Chemical and Structural Characterizations of the Holm Oak-Derived Lignin Binder

Prior the extraction, the compositional analysis of the holm oak feedstock has been performed in order to primarily assess the lignin content (Table 3). Since Holm Oak waste used in this work is composed of wood and bark, the extractives content in the form of waxes, resins, gums, soluble sugars, starches, etc. is expected to be relevant, and higher than that of bark-free samples. The total amount of lignin, expressed as the sum of Klason lignin and acid soluble lignin, is here 29.2 % and comparable with that of other woody precursors in the literature.[37] The acid soluble lignin, which is generally composed by the low-molecular weight fraction of lignin,[47] represents a small fraction of the holm oak total lignin content, and is expected to deteriorate the performance of lignin when used as binder material for SIBs, since low-molecular weight fraction can be solubilized in electrolyte solvents.

The extraction of lignin binder was performed using the organosolv separation method described in Section 2.2. The organsolv-based separation of the different components of the biomass involves the breaking of lignin-carbohydrate complexes (LCC) linkages, followed by the hydrolysis of glycosidic bonds of hemicellulose and depolymerization of lignin through the cleavage of ether bonds, promoting the dissolution of lignin.[48] In this way, an insoluble cellulose-rich fraction in the solid residue and an organosolv liquor containing both lignin and water-soluble compounds, such as sugars (mainly hemicellulose monomers) and carbohydrates decomposition products, are obtained.[49]

Table 3 Holm Oak feedstock macromolecular composition.

Extractives %	Klason Lignin %	Acid Soluble Lignin %	Holocellulose %	Ash %
11.4	21.6	7.6	58.1	1.3

The lignin in the filtrate is separated through the addition of fresh water which promotes its precipitation.[32] The process is schematized in Figure 3. The isolated lignin yield, calculated with respect to the weight of the starting biomass, was 13.9 %: this means that around the 48 % of the total lignin content in holm oak, and 64 % of the acid insoluble lignin can be recovered by precipitation. The effectiveness of lignin dissolution can be explained with the Hildebrand and especially the Hansen solubility parameters (δ). The Hildebrand δ of lignin ranges between 21.0 and 25.0 $MPa^{1/2}$ [50] while that of GVL is 23.1 $MPa^{1/2}$.[31] Therefore, according to the Hildebrand parameters, GVL has an high affinity for lignin.-However, for polar molecules such as GVL, Hansen Solubility Parameters (HSP) are more realistic since they take into account the contribution of hydrogen bond ability and polar nature of the molecules.[49] According to the Hansen theory, a practical way to evaluate how close each other are the solubility parameters of two substances is the calculation of the Hansen Relative Energy Difference (RED), which is a parameter describing the compatibility between solvent and solute, of which details and calculations are reported elsewhere.[51] Briefly, a good solvent

has a RED value lower than 1, while bad solvent has a RED value higher than 1. In this case, the Hansen relative energy difference between lignin and GVL is 0.83,[52] thus indicating that the solvent is able to solubilize lignin. Moreover, the RED value of GVL and lignin reaches 0.58 when a mixture 80 % GVL and 20 % of H_2O is used.[30] These results are the consequence of the enhanced hydrogen bonding capability of the solvent system, which allows easier and stronger hydrogen bonding interactions between solvent system and lignin, replacing the intermolecular hydrogen bonds in lignin and therefore promoting the dissolution.[53] Although according to the Hansen RED the optimal solubility should be reached at GVL 80 % and H_2O 20 %, experimental results show that the maximum extent of lignin dissolution was obtained using water content in the range 35-50 %.[31,32] These results can be related to the higher H-bonding ability, which is maximum at GVL concentration between 50-60 %, providing more hydrogen bonds respect to pure GVL , but excessive water makes the interaction between γ-valerolactone and water molecules stronger, hindering the formation of hydrogen bonds with lignin.[54,55]

In order to estimate the purity of the isolated lignin, Klason Lignin, acid soluble lignin and ash content percentages were measured according to the TP-510-42618 protocol. As shown in Table 4, the purity of recovered lignin was estimated as 95.2 % (85.5 % if only Klason lignin is considered). The purity of the obtained lignin is in the range of other organosolv lignins isolated using different raw materials and solvents.[56–58] Ash and residual carbohydrates impurities are below 5 %.

Table 4 Chemical composition of lignin recovered from the organosolv liquor.

Klason Lignin %	Acid Soluble Lignin %	Total Lignin %	Ash %	Others %
85.5	9.7	95.2 %	0.7	4.1

FT-IR spectra of extracted lignin is shown in Figure 4a, while the respective peaks assignments are summarized in Table S1. The broad band between 3550–3100 cm^{-1} is attributed to the O-H stretching of phenolic and alcoholic groups.[26] The peaks at 2938 cm^{-1} and 2837 cm^{-1} are attributed to C-H stretching in -CH_2- and -CH_3, respectively. The band with two ticks at around 1730 cm^{-1} can be assigned to the C=O stretching of the residual acetyl group of hemicellulose[52] and to the unconjugated carbonyl group.[57] In the region of aromatic backbone vibrations (~ 1600-1250 cm^{-1}), different peaks with different intensities are evidenced. Syringyl units (S) of lignin show typical bands at 1595 cm^{-1}, 1326-1324 cm^{-1} and 1110 cm^{-1}, which are assigned to the aromatic skeletal vibrations, S ring breathing and aromatic C-H in plane deformation of S units, respectively. On the other hand, guaiacyl units (G) of lignin exhibit the above-mentioned vibrations with bands at 1524 cm^{-1}, 1257 cm^{-1} and 1030 cm^{-1}, respectively.[58] The band at 1219 cm^{-1} is attributed to the C-O stretching of characteristic aryl and alkyl ether linkages of lignin. The thermal behavior of the isolated lignin was characterized using thermogravimetric analysis (Figure 4b). Generally, lignin has an high thermal stability and decomposes slowly in a wide temperature range from room temperature to 800 °C, leaving a considerable amount of solid residue.[59] Nonetheless, different stages of degradation can be distinguished. At the first stage (around 100 °C), the weight losses can be attributed to the moisture retained in the samples. The next stage, which occurs in the temperature range 180-300 °C and leads to a weight loss of around 17.4 %, can be attributed either the degradation of carbohydrates residual impurities in the lignin sample, which are converted to volatile gases such as CO, CO_2, and CH_4, or to the start of lignin decomposition. The latter becomes the uppermost phenomenon in the temperature range 300-450 °C, where the fragmentation of inter-unit linkages releases monomers and low-molecular weight derivatives of phenol into the vapor phase,[60] producing a weight loss of 21.1 %. As the temperature is further increased (over 450 °C), the decomposition and condensation of aromatic rings occurs, leading to the formation of char, which gives a solid residues of around 36 %.[52,60] Finally, the molecular weight distribution of the derivatized lignin sample has been measured with GPC. The calculated number-average molecular weight (M_n), weight-average molecular weight (M_w) and polydispersity index (PDI) are reported in Table S2. The vertical and dotted lines in Figure 4c the represent the elution times for some of the polystyrene molecular weight standards used for the calibration. The broad curve in GPC chromatogram and the PDI value of 2.6 reflect the heterogeneity among lignin chain lengths, as result of the simultaneous occurrence of lignin depolymerization and recondensation reactions during GVL organosolv extraction.[30] The weight-average molecular weight M_w was estimated to be 2156 g mol^{-1}, which is well below the typical range of milled wood lignin (5500 – 20000 g mol^{-1}).[24] This suggests that the reaction severity, i.e. reaction temperature and time, largely promote depolymerization reactions. Overall, the obtained M_w and M_n are comparable with other lignins extracted by GVL from different biomasses (Table S2).

3.3 Electrochemical Characterizations

Cyclic Voltammetry (CV) during the initial three cycles was performed on holm oak-derived hard carbon coupled with lignin binder in order to assess the topotactical reaction of Na^+ in LHC. The analysis was performed at a scanning rate of 0.10 mV s^{-1} in the potential range 0.01 < E_{we} < 2.00 V using metallic sodium as reference and counter electrodes. As shown in Figure 5a, during the first cathodic scan, an irreversible broad peak (A) extends from approximatively 1.00 V to 0.20 V, and can be assigned mainly to the decomposition of the electrolyte and the formation of the SEI, which is the main responsible of low ICE.[61] In the following scans, the contribution from irreversible SEI formation disappears, leaving a reversible broad peak (B) at potential values between 0.90 and 0.10 V and a narrow and reversible peak (C) centered at around E_{we} = 0.01 V. Although there is still an ongoing debate regarding the sodium storage mechanism into hard carbon, the broader-potential-range feature marked as B may be largely associated to the adsorption of sodium ions at surface active sites,[62] while the low-voltage peak may be mainly attributed to the Na^+ intercalation into hard carbon graphene layers. Also, a contribution of pseudocapacitive processes related to the internal pores filling by Na must be take into account especially at potentials approaching the cut-off of 0.01 V. [63] During the anodic scans, the oxidation peaks (C') and the broad feature (B') indicate the reversibility of the electrochemical processes. After the 1st cycle, the CV curves are overlapped, confirming the reversibility of processes described by the B/B' and C/C' features. To further investigate the Na storage mechanism of hard carbon, cyclic voltammetries were recorded and different scan rates between 0.1 mV s^{-1} and 1.0 mV s^{-1} (Figure S1a) and the power-law relationship was used to discriminate between surface-controlled and diffusion-controlled reactions by fitting the experimental data to the following equation (eqn.4):[64]

View Article Online
DOI: 10.1039/D5SE00645G

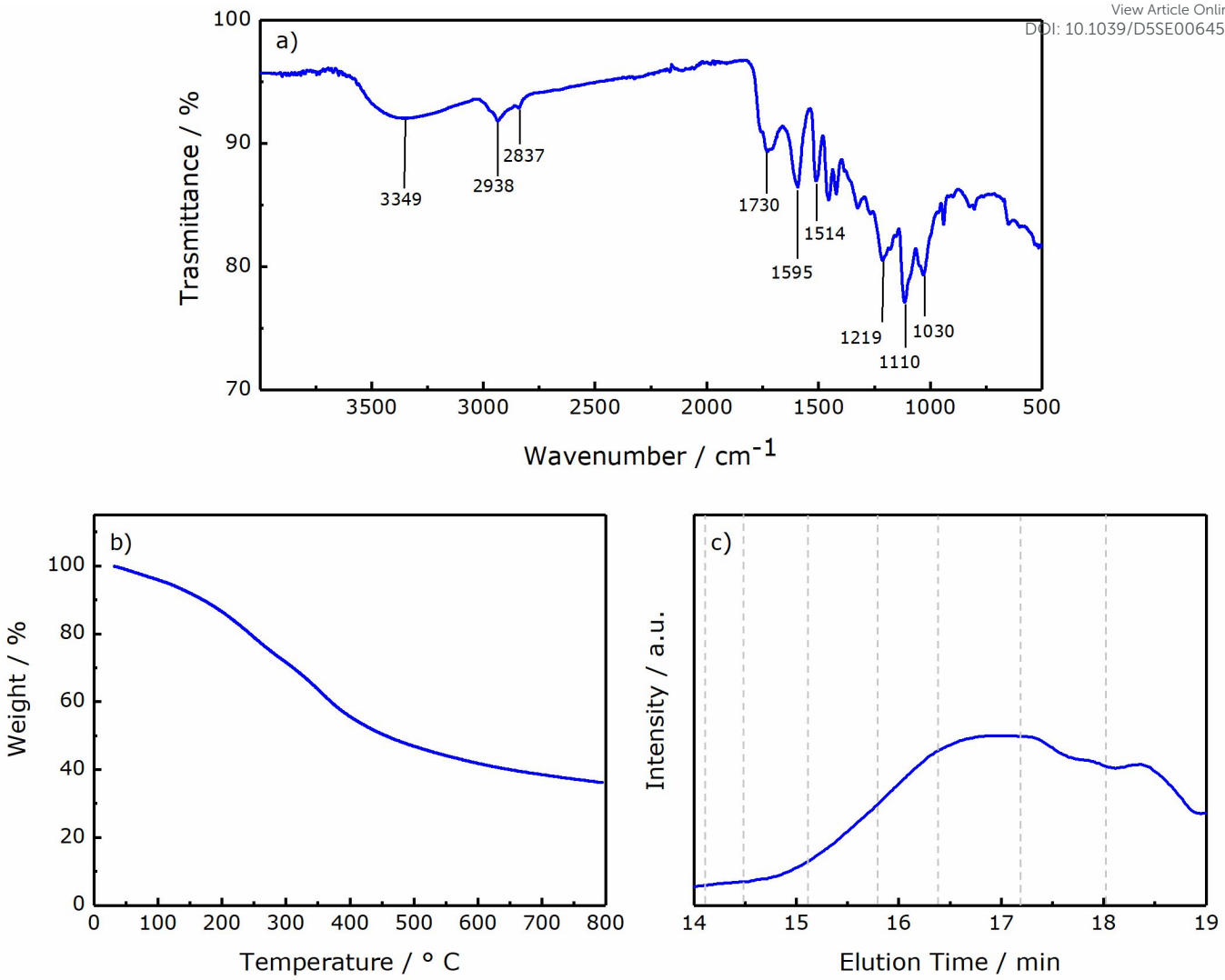

Figure 4 Characterizations of holm oak extracted lignin: (a) FT-IR spectra; (b) TGA analysis; (c) GPC chromatogram.

$$i = a v^b \quad (4)$$

Where i is the peak current, v is the scanning rate, while a and b are constants that has to be determined. The b value can be obtained by calculating the slope of the linear fit of log i vs log v according to the eqn. (5):

$$\log i = b \log v + \log a \quad (5)$$

Typically, a value of b close to 0.5 indicates a diffusion-controlled reaction, while a value of b close to 1 indicates that the current is controlled by a capacitive behavior. Here, two peaks were considered: the first one is the broad peak at 0.5 V (i_s) corresponding to the sloping region, while the second one is the sharp peak in the low potential region at 0.01 V (i_p). Figure S1b shows the excellent linear relationship ($R^2 = 0.99$) for both curves between current peaks and scan rate in logarithmic scale. The obtained b-values were 0.84 for i_s and 0.54 for i_p, respectively. Thus, these results suggests that the current in the sloping region (i_s) mostly arises from the surface-controlled reactions, such as adsorption on surface active sites, while the current at low-potentials (i_p) originates from the diffusion-controlled reaction (i.e. sodium insertion/extraction between graphene layers). Additionally, the capacitive contribution to the current response can be determined according to the following equation (eqn. (6)):

$$i(V) = k_1 v + k_2 v^{1/2} \quad (6)$$

where the current response at a fixed potential can be differentiate in capacitive-controlled ($k_1 v$) and diffusion-controlled ($k_2 v^{1/2}$) contributions. The contribution of the two mechanisms to the current response can be determined counting k_1 and k_2.[65] Figure S1c shows the trends of capacitive and diffusive contributions (%) as a

function of potential (V) at scan rate of 0.1 mV s^{-1}. As expected, during sodiation, the capacitive contribution % is maximum at 0.75 V (81.5 %) and then progressively decreases reaching a minimum at 0.05 V (19.4 %). These results suggest that at low-potential ($E_{we} \leq$ 0.15 V) the main process is the diffusion-controlled intercalation of Na^+ into hard carbon with a non-negligible contribution of pseudocapacitive process, while in the sloping region ($0.35 \leq E_{we} \leq$ 0.75 V) pseudocapacitive processes govern the charge storage. The galvanostatic charge and discharge profiles E vs. Q of LHC-LGN composite electrode, cycled at current density of 300 mA g^{-1} in the potential range $0.01 < E_{we} < 2.00$ V shown in Figure 5b, confirm the typical pattern of hard carbon Na storage evidenced by CV. In fact, a pseudo-plateau starting at around 0.80 V (corresponding to broad peak A in CV), due to the electrolyte decomposition and solid electrolyte interphase (SEI) formation, is evidenced.[10] The associated irreversible capacity loss is remarkable (around 273 mAh g^{-1}) corresponding to an ICE of 42 %. As in CV, this feature disappears in the subsequent cycle indicating that a relatively stable SEI is formed[40] and no additional parasitic reactions occurs . On the other side, the sloping potential profiles approximatively between 0.80 and 0.10 V during reduction and between 0.30 and 1.00 V during oxidation (corresponding to B/B' broad features in CV) and the low-potentials plateau (corresponding to C/C' narrow peaks in CV), are highly reversible upon cycling. This confirms the reversibility of the sodium uptake/removal as well as the maintenance of electrode integrity, as demonstrated by the capacity retention of 91.1 % at 100th cycles. Figure 5c details the charge/discharge behavior over 100 cycles. The electrode delivers a discharge capacity of 496.0 mAh g^{-1} which decreases in the second discharge to 215.5 mAh g^{-1}. The irreversible electrolyte decomposition and Na^+ ion trapping into HC matrix led to a poor ICE % of 38.9 %.[66] One explanation of this poor ICE can be found both in the high specific surface area of the holm oak-derived HC, which inevitably offers a large exposed surface to the electrolyte decomposition, and also in the high concentration of surface defects, particularly oxygen-containing functional groups revealed by the EDX analysis of LHC, which are able to promote the decomposition of the electrolyte.[67,68] Nonetheless, the LHC-LGN composite electrode exhibit a progressive increases in the reversibility of the sodiation/desodiation process after 10 cycles, since the specific capacity tends to stabilize at about 180 mAh g^{-1}. The cell retains the 90.6 % of the capacity after 100 cycles. In order to evaluate the impact of lignin binder on the electrochemical performances of the hard carbon electrode, a comparison of the cycling performances of the LHC-LGN composite electrode with two well-established binders (PVDF and CMC) have been carried out. As shown in Figure S2 and detailed in Table S3, all the three electrodes display poor ICE % values, where lignin-based electrode exhibits the lowest ICE % (38.9 %) followed by PVDF (42.6 %) and CMC (45.3 %). These results suggest that the binder has a relative impact on the decomposition of the electrolyte since no significative variations are encountered between these different binders. Therefore, the high SSA of LHC active material can be recognized as the main responsible of low ICE %. However, for the sake of clarity, the average coulombic efficiencies of all cells are yet not adequate for real practical application since no one reach values above 99.5 %, where that of LGN-based electrode is in the range 97-98 %. This could be ascribed either to limitations coming from the half-cell setup (i.e. presence of Na metal rather than a cathode) and to the lab-scale electrode manufacture which can underestimate the electrochemical performances of the cell and in particular its stability. However, these aspects and can be carefully optimized during scale-up and full cell optimization.[69] Indeed, not even the CMC- and PVDF-based electrodes reach satisfactory coulombic efficiencies, with the latter also encountering capacity fluctuations after around 55 cycles probably ascribed to the instability of the electrode/electrolyte interface. Nonetheless, the specific capacity and capacity retention of lignin-based electrode is comparable with those obtained with PVDF- and CMC-based electrodes, which are of great importance for further developments. To deeply assess the electrochemical performances of holm oak-derived hard carbon with γ-valerlactone extracted lignin binder, a rate capability test was performed at selected cycling rates in the range C/10 to 5C, as shown in Figure 5d. The poor coulombic efficiency of initial low-current rates cycles is the results of the favored electrolyte decomposition at slow kinetics.[70] Nonetheless, the LHC-LGN exhibits a promising rate capability experimenting low-capacity fade when the current is increased. The average discharge capacities are of 315.9, 243.1, 215.5, 198.9, 180.7 mAh g^{-1} at C/5, C/2, 1C, 2C and 5C, respectively. Moreover, restoring the current to 1C up to 100 overall cycles yields a specific capacity above 190 mAh g^{-1} after 100 cycles, with a reversibility of the charge/discharge processes at 1C (300 mA g^{-1}) in line with that already evidenced in Figure 5c. In order to further evaluate the ability of lignin binder to guarantee long cycle life even in demanding conditions, galvanostatic cycles were performed on LHC-LGN composite electrodes at current densities of 900 mA g^{-1} (3C) and 1500 mA g^{-1} (5C). As shown in Figure 5 e,f, in both conditions the LHC-LGN cells are characterized, during the initial cycles, by a low coulombic efficiency due to SEI formation at hard carbon surface. Nonetheless, after cell activation, both cells deliver high specific reversible capacities (220.0 and 213.3 mAh g^{-1} at 3C and 5C, respectively), as well as long cycling stability, as demonstrated by capacity retention values of 86.8 % and 83.7 % after 100 cycles and 79.1 % and 71.6 % after 500 cycles for cell cycled at 3C and 5C, respectively. It should be noted that, in any cycling conditions at 1C, 3C and 5C, no spikes in desodiation capacity, ascribable to possible SEI dissolution/reformation, are evidenced, suggesting a long-term stability of the passivation layer. Relevant results are summarized in Table 7. Overall, all these results suggest the ability of lignin binder to guarantee the electrode integrity during cycling, ensuring high-capacity retention and long cycle life. Taking into account the relatively low molecular weight measured for the extracted lignin, the good binding ability of lignin binder is not expected to be given only by the mechanical interlocking mechanism such as in PVDF, but more plausibly and at larger extent by the intermolecular forces, especially the H-bonds between the polar functional groups of lignin and the oxygen-containing functional groups of hard carbon.[71]

Table 7 First cycle discharge capacities, initial coulombic efficiencies %, second cycle discharge capacities and capacity retentions after 100 cycles of LHC-LGN composite electrodes at different current rates.

Electrode	Discharge Capacity 1st cycle (mAh g^{-1})	ICE (%)	Discharge Capacity 2nd cycle (mAh g^{-1})	Capacity Retention after 100 cycles (%)
1C	496.0	38.9	215.5	90.6
3C	575.8	35.6	220.0	86.8
5C	509.5	38.8	213.3	83.7

Additional information about the electrode integrity after 100 cycles was obtained performing SEM morphological investigation of pristine and cycled electrode (Figure 6 a,b). Inevitably, the morphology of the pristine electrode shows different textures with respect to the cycled one, in light also of the different spots analyzed. However, the rough and inhomogeneous surface of the pristine electrode can be considered maintained after cycling, since no significative morphological changes can be detected in the cycled electrode. Noteworthy, the cycled electrode does not display visible cracks confirming the electrode integrity and the ability of the lignin binder to guarantee longstanding adhesion.

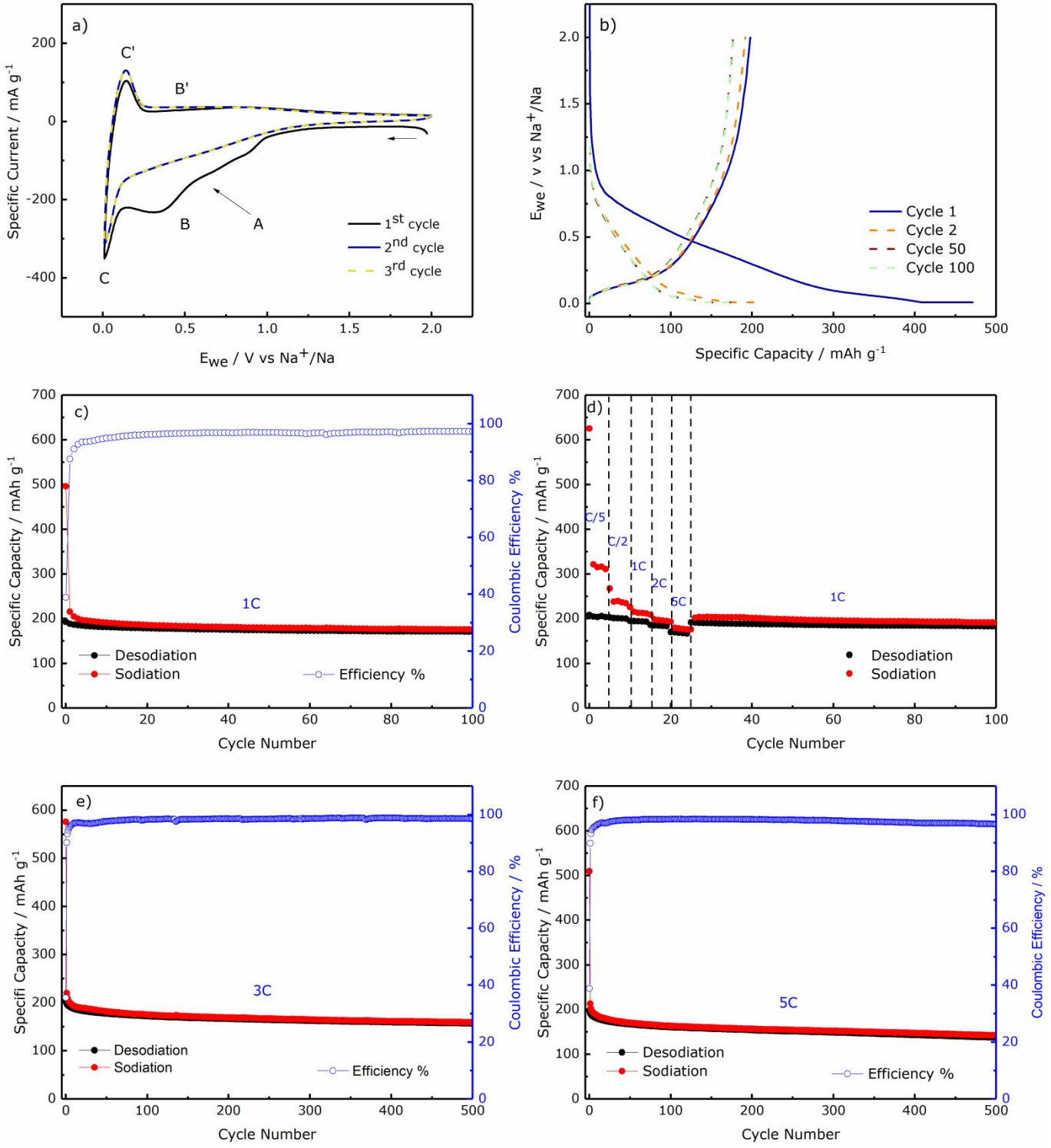

Figure 5 Electrochemical characterization of LHC-LGN composite electrode in Na half-cells: (a) Cyclic Voltammetry upon the first three cycles at a scan rate of 0.1 mV s^{-1}; (b) Galvanostatic profiles of charge/discharge of cell cycled at 1C; (c) Cycling at 1C; (d) Rate capability; (e) Long cycling at 3C and (f) Long cycling at 5C.

To better investigate the electrode kinetics and electrode/electrolyte interfacial behavior of the LHC-LGN composite electrode, potentiostatic impedance spectroscopy measurements were performed at the second cycle and every 10th cycle at E_{we} = 0.4 V upon sodiation. The bias potential to be applied during impedance measurements has been evaluated by the inspection of dQ dE^{-1} differential curves (obtained by differentiating the electrode galvanostatic profiles at different cycles). As shown in Figure 7a, a potential E_{we} = 0.40 V has been chosen, where the voltage oscillations applied during the impedance measurements are expected to produce limited current oscillations. As a consequence, the system is expected to respect the pseudolinearity, causality and stationarity boundary conditions required for meaningful impedance measurements. The obtained Nyquist plots are shown in Figure 7b. All the impedance spectra are characterized by an intercept with real axis in the high frequency region, a first semicircle in the high- to medium- frequency region, a second semicircle in the middle- to low-frequency region and a straight line in the low-frequency region. EIS data were modeled through an equivalent circuit model, noted as $R_{el}(R_{SEI}C_{SEI})(R_{ct}C_{dl})WC_i$ in Boukamp's notation.

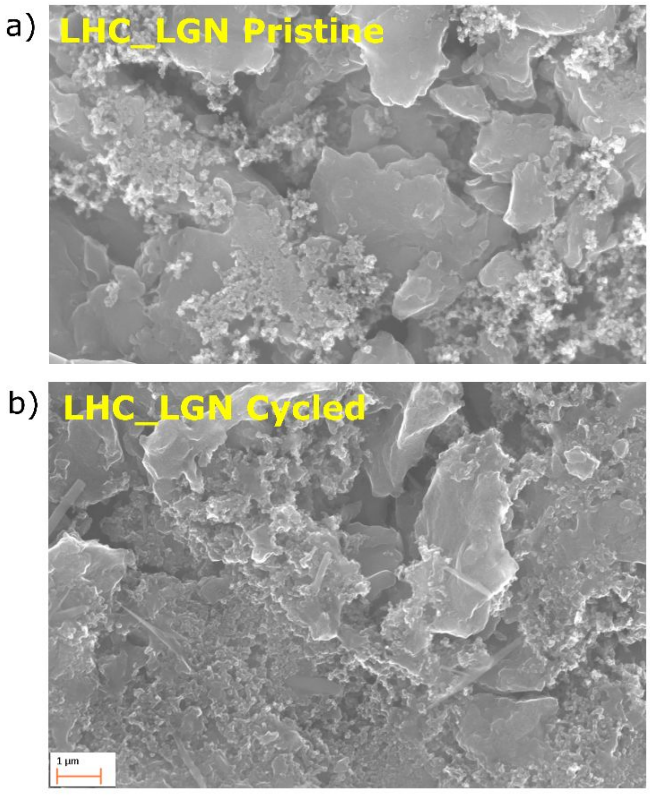

Figure 6 SEM images of pristine and cycled electrodes**.** Magnification 20000x.

In details, the intercept with real axis describes the Na^+ migration through the electrolyte and has been modeled as a pure resistive element R_{el}; the first semi-circle represents the Na^+ migration through the SEI layer, involving charge accumulation around its surface, hence it was modeled with a resistive element (R_{SEI}) in parallel with a capacitive element (C_{SEI}); the second semi-circle can be ascribed to the faradaic charge transfer process, which is accompanied by the electric double layer at active material/electrolyte interface, thus was modeled with a resistive element (R_{ct}) in parallel with a capacitor (C_{dl}); finally, the low frequency line describes a semi-infinite diffusion to a blocking electrode and it was modeled as a Warburg impedance element (W) in series with a capacitor (C_i) indicating the intercalation capacitance. The values of the parameters related to the model circuit elements were calculated by performing a nonlinear least square (NLLS) fitting with Relaxis3 software, where the pure capacitive elements were replaced by constant-phase elements Q to take into account electrode surface roughness and inhomogeneity.[72] The trends of the calculated R_{el}, R_{SEI} and R_{ct} upon cycling are shown in 7c, while the respective numerical values of resistances are detailed in Table 8. Only NLLS fits of Nyquist plot with χ^2 in the order of 10^{-4} or below were reported.[73] Beyond the electrolyte resistance (R_{el}), which is stable throughout the cycling, the LHC-LGN electrode shows an initial increase of SEI resistance indicating the progressive formation of the passivation layer at electrode/electrolyte interface. After 10 cycles, there is a stabilization of R_{SEI} suggesting that the formation of a stable SEI has been completed, which prevents further electrolyte decomposition. This trend is consistent with the results obtained during galvanostatic cycling (Figure 5 c,e), where the irreversible contributions to capacity progressively decreases during the first cycles, while the coulombic efficiencies increase as a consequence of SEI formation.

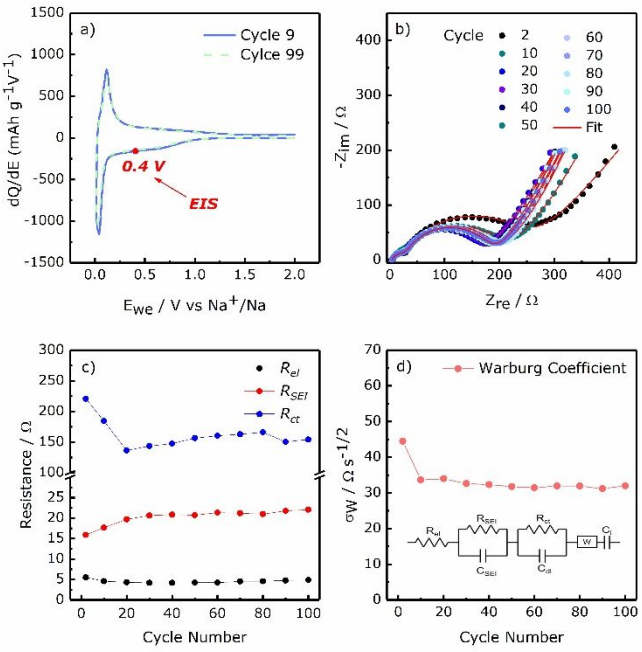

Figure 7 (a) dQ dE^{-1} vs E_{we} curves at different cycles;(b) Nyquist plot of LHC-LGN electrode acquired at second cycle and every 10th cycle, E_{we} = 0.4 V, 100 kHz > f > 10 mHz; (c) Values of R_{el}, R_{SEI} and R_{ct} upon cycling, as obtained by EIS data analysis; (d) Warburg Coefficient values as a function of cycle number; Inset: Equivalent circuit used to simulate the data;

Table 8 Numerical values of R_{el}, R_{SEI}, R_{ct} and the corresponding χ^2obtained during NLLS analysis.

Cycle Number	R_{el} (Ω)	R_{SEI} (Ω)	R_{ct} (Ω)	χ^2
2	5.49	15.91	220.58	3×10^{-4}
10	4.56	17.65	184.46	3×10^{-5}
20	4.31	19.70	136.41	7×10^{-5}
30	4.20	20.63	143.65	5×10^{-5}
40	4.18	20.86	147.80	5×10^{-5}
50	4.21	20.73	156.64	4×10^{-5}
60	4.20	21.31	160.30	3×10^{-5}
70	4.51	21.20	163.05	4×10^{-5}
80	4.57	20.99	166.11	5×10^{-5}
90	4.72	21.77	150.48	6×10^{-5}
100	4.85	22.07	154.29	6×10^{-5}

On the other hand, the charge-transfer resistance R_{ct} sharply decreases during first 20 cycles, probably as a consequence of the electrode activation due to progressive pore surface wetting by the electrolyte. Then, the R_{ct} tends to stabilize around 150 Ω, revealing a stabilization of reaction kinetics at electrode/electrolyte interface. The impedance results explain both the good rate capability and cycling stability obtained for LHC-LGN electrodes cycled at different current rates. Finally, the Warburg coefficient σ_W (Figure 7d) decreases from cycle 2 to cycle 10 and then remain almost constant upon cycling, indicating a stable solid-state diffusion of Na^+ ions into the bulk of the electrode. This trend suggests that, after interface activation and SEI formation, no particle agglomeration or other significative textural changes occurs in the LHC-LGN electrode during cycling.

4. Conclusions

In this work, the feasibility of use holm-oak as feedstock for the preparation of electrode materials for sodium-ion batteries have been demonstrated. Hard carbon has been synthesized by a one-step pyrolysis followed by acid leaching to remove the inorganic impurities. The chemical, structural and morphological characterizations revealed that the obtained hard carbon possesses a low atomic percentage of heteroelements (mostly oxygen) and high interlayer distance (0.392 nm), which is favorable for sodium insertion/extraction; moreover, it has an high SSA and well-developed microporosity, which are beneficial for sodium pseudocapacitive storage but detrimental for the initial coulombic efficiency of the electrode. In parallel, lignin sample was extracted by organosolv method using γ-valerolactone:water mixture and then used as binder material. The performed extraction allows to precipitate no more than 64 % of the total lignin in the raw material. Nonetheless, the obtained lignin is characterized by high level of purity and relatively low molecular weight, suggesting that the binding ability is mainly provided via chemical bonding such as the H-bonds between the polar functional groups of lignin and the oxygenated surface functional groups of hard carbon, establishing strong interactions. When the two materials are combined in an anode for SIBs, they exhibit good electrochemical performances delivering specific capacities of around 200 mAh g^{-1} and long cycling stabilities at different current rates. These behaviors were corroborated by the SEM images before and after cycling and through impedance spectroscopy analysis during cycling. The former confirms the electrode integrity, with no visible particle agglomeration and morphological changes, while the latter mainly evidences the electrode/electrolyte interface stability and almost constant reaction kinetics during cycling. Overall, these results show that both hard carbon, with excellent Na storage performance, and lignin binder, with longstanding adhesion, can be developed from natural sources such as holm oak waste in environmentally-friendly and cost-efficient ways. Nonetheless, future works can be aimed to assessing the suitability of use lignin binder at cathode side, where the replacement of PVDF and NMP-processing currently represents an open challenge. Indeed, the water sensitivity of typical cathode materials, i.e. layered oxides, do not allow to use the water-soluble sodium carboxymethylcellulose (CMC), which also suffers of small electrochemical stability window, inherently hindering the use of high-voltage layered oxide cathodes in SIBs.

Author contributions

All the authors contributed to this work and approved the final version of the manuscript. L.B., F.N., A.C and S.G. conceptualized the work. L.B and F.N. wrote the manuscript draft. L.B., H.D., F.V. and G.P. performed the laboratory activities. L.B., H.D., L.S., A.S., L.M. contributed to the analysis and discussion.

Data availability

All the produced data are available within this manuscript.

Conflicts of interest

There are no conflicts to declar.

Acknowledgements

Authors acknowledge financial support from projects "ORgANics for Green Electrochemical Energy Storage Project (ORANGEES)", funded by MASE "PT 2019-2021, DD 27.10.2021 bando a, DD 05.08.2022" and "Green Electrolyte and Biomass-derived Electrodes for Sustainable Electrochemical Storage Devices (GENESIS)", funded by Ministero dell'Università e della Ricerca, within the PRIN 2022 program (DD 104 02.02.2022).

References

1 J. Janek and W. G. Zeier, *Nat. Energy*, 2016, **1**, 1–4.
2 K. W. Beard and T. B. Reddy, *Linden's Handbook of Batteries*, McGraw-Hill, New York, 2019.
3 J. Deng, C. Bae, A. Denlinger and T. Miller, *Joule*, 2020, **4**, 511–515.
4 B. E. Lebrouhi, S. Baghi, B. Lamrani, E. Schall and T.

Kousksou, *J. Energy Storage*, 2022, **55**, 105471.
5 H. Pan, Y. S. Hu and L. Chen, *Energy Environ. Sci.*, 2013, **6**, 2338–2360.
6 V. Palomares, P. Serras, I. Villaluenga, K. B. Hueso, J. Carretero-González and T. Rojo, *Energy Environ. Sci.*, 2012, **5**, 5884–5901.
7 T. Liu, Y. Zhang, Z. Jiang, X. Zeng, J. Ji, Z. Li, X. Gao, M. Sun, Z. Lin, M. Ling, J. Zheng and C. Liang, *Energy Environ. Sci.*, 2019, **12**, 1512–1533.
8 TRADING ECONOMICS, https://tradingeconomics.com/.
9 I. Hasa, J. Barker, G. Elia and S. Passerini, *Sodium-ion batteries: History, development, and overview on market and application*, Elsevier B.V., 2nd edn., 2023.
10 L. Bottoni, H. Darjazi, L. Sbrascini, A. Staffolani, S. Gabrielli, G. Pastore, A. Tombesi and F. Nobili, *ChemElectroChem*, 2023, **10**, 1–11.
11 J. Y. Hwang, S. T. Myung and Y. K. Sun, *Chem. Soc. Rev.*, 2017, **46**, 3529–3614.
12 X. Chen, C. Liu, Y. Fang, X. Ai, F. Zhong, H. Yang and Y. Cao, *Carbon Energy*, 2022, 1–18.
13 J. Górka, C. Vix-Guterl and C. Matei Ghimbeu, *C*, 2016, **2**, 24.
14 U. Mittal, L. Djuandhi, N. Sharma and H. L. Andersen, *JPhys Energy*, , DOI:10.1088/2515-7655/ac8dc1.
15 K. L. Hong, L. Qie, R. Zeng, Z. Q. Yi, W. Zhang, D. Wang, W. Yin, C. Wu, Q. J. Fan, W. X. Zhang and Y. H. Huang, *J. Mater. Chem. A*, 2014, **2**, 12733–12738.
16 J. Gupta, M. Kumari, A. Mishra, Swati, M. Akram and I. S. Thakur, *Chemosphere*, 2022, **287**, 132321.
17 F. Wang, D. Ouyang, Z. Zhou, S. J. Page, D. Liu and X. Zhao, *J. Energy Chem.*, 2021, **57**, 247–280.
18 S. L. Chou, Y. Pan, J. Z. Wang, H. K. Liu and S. X. Dou, *Phys. Chem. Chem. Phys.*, 2014, **16**, 20347–20359.
19 D. Bresser, D. Buchholz, A. Moretti, A. Varzi and S. Passerini, *Energy Environ. Sci.*, 2018, **11**, 3096–3127.
20 S. Nayak, G. Sahoo, I. I. Das, A. K. Mohanty, R. Kumar, L. Sahoo and J. K. Sundaray, *Toxics*, , DOI:10.3390/toxics11060543.
21 X. Lim, *Nature*.
22 Y. Zhang and M. Naebe, *ACS Sustain. Chem. Eng.*, 2021, **9**, 1427–1442.
23 W. J. Chen, C. X. Zhao, B. Q. Li, T. Q. Yuan and Q. Zhang, *Green Chem.*, 2022, **24**, 565–584.
24 A. Beaucamp, M. Muddasar, I. S. Amiinu, M. Moraes Leite, M. Culebras, K. Latha, M. C. Gutiérrez, D. Rodriguez-Padron, F. del Monte, T. Kennedy, K. M. Ryan, R. Luque, M. M. Titirici and M. N. Collins, *Green Chem.*, 2022, **24**, 8193–8226.
25 J. M. Yuan, W. F. Ren, K. Wang, T. T. Su, G. J. Jiao, C. Y. Shao, L. P. Xiao and R. C. Sun, *ACS Sustain. Chem. Eng.*, 2022, **10**, 166–176.
26 H. Lu, A. Cornell, F. Alvarado, M. Behm, S. Leijonmarck, J. Li, P. Tomani and G. Lindbergh, *Materials (Basel).*, 2016, **9**, 1–17.
27 T. Chen, Q. Zhang, J. Pan, J. Xu, Y. Liu, M. Al-Shroofy and Y. T. Cheng, *ACS Appl. Mater. Interfaces*, 2016, **8**, 32341–32348.
28 C. Luo, L. Du, W. Wu, H. Xu, G. Zhang, S. Li, C. Wang, Z. Lu and Y. Deng, *ACS Sustain. Chem. Eng.*, 2018, **6**, 12621–12629.
29 R. Gond, H. D. Asfaw, O. Hosseinaei, K. Edström, R. Younesi and A. J. Naylor, *ACS Sustain. Chem. Eng.*, , DOI:10.1021/acssuschemeng.1c05263.
30 X. Xu, K. Wang, Y. Zhou, C. Lai, D. Zhang, C. Xia and A. Pugazhendhi, *Fuel*, 2023, **338**, 127361.
31 H. Q. Lê, A. Zaitseva, J. P. Pokki, M. Ståhl, V. Alopaeus and H. Sixta, *ChemSusChem*, 2016, **9**, 2939–2947.
32 W. Fang and H. Sixta, *ChemSusChem*, 2015, **8**, 73–76.
33 A. Sluiter, R. Ruiz, C. Scarlata, J. Sluiter and D. Templeton, *Natl. Renew. Energy Lab.*, 2008, 9.
34 A. Sluiter, B. Hames, R. Ruiz, C. Scarlata, J. Sluiter, D. Templeton and D. Crocker, *Natl. Renew. Energy Lab.*, 2008, 17.
35 C. Nita, B. Zhang, J. Dentzer and C. Matei Ghimbeu, *J. Energy Chem.*, 2021, **58**, 207–218.
36 A. Beda, J. M. Le Meins, P. L. Taberna, P. Simon and C. Matei Ghimbeu, *Sustain. Mater. Technol.*, , DOI:10.1016/j.susmat.2020.e00227.
37 C. del Mar Saavedra Rios, L. Simonin, C. M. Ghimbeu, C. Vaulot, D. da Silva Perez and C. Dupont, *Fuel Process. Technol.*, 2022, **231**, 107223.
38 D. E. Newbury and N. W. M. Ritchie, *Scanning*, 2013, **35**, 141–168.
39 A. Kamiyama, K. Kubota, T. Nakano, S. Fujimura, S. Shiraishi, H. Tsukada and S. Komaba, *ACS Appl. Energy Mater.*, 2020, **3**, 135–140.
40 V. Velez, G. Ramos-Sánchez, B. Lopez, L. Lartundo-Rojas, I. González and L. Sierra, *Carbon N. Y.*, 2019, **147**, 214–226.
41 L. Sbrascini, A. Staffolani, L. Bottoni, H. Darjazi, L. Minnetti, M. Minicucci and F. Nobili, *ACS Appl. Mater. Interfaces*, , DOI:10.1021/acsami.2c07888.
42 D. Mp, M. Misra and A. K. Mohanty, *Environ. Sci. Adv.*, 2023, **2**, 1282–1301.
43 M. Bartoli, A. Piovano, G. Antonio, G. Meligrana, C. Tealdi, G. Pagot, E. Negro, R. Pedraza, C. Triolo, L. Vazquez, N. Comisso, A. Tagliaferro, S. Santangelo, E. Quartarone, V. Di, P. Mustarelli, R. Ruffo and C. Gerbaldi, *Renew. Sustain. Energy Rev.*, 2024, **194**, 114304.
44 S. Puravankara and Nagmani, *ACS Appl. Energy Mater.*, 2020, **3**, 10045–10052.
45 K. Yu, X. Wang, H. Yang, Y. Bai and C. Wu, *J. Energy Chem.*, 2021, **55**, 499–508.
46 C. Matei Ghimbeu, J. Górka, V. Simone, L. Simonin, S. Martinet and C. Vix-Guterl, *Nano Energy*, 2018, **44**, 327–335.
47 J. Domínguez-Robles, T. Tamminen, T. Liitiä, M. S. Peresin, A. Rodríguez and A. S. Jääskeläinen, *Int. J. Biol. Macromol.*, 2018, **106**, 979–987.
48 Y. Li, Y. Liu, W. Chen, Q. Wang, Y. Liu, J. Li and H. Yu, *Green Chem.*, 2016, **18**, 1010–1018.
49 Z. Zhang, M. D. Harrison, D. W. Rackemann, W. O. S. Doherty and I. M. O'Hara, *Green Chem.*, 2016, **18**, 360–381.
50 R. Rinaldi, R. Jastrzebski, M. T. Clough, J. Ralph, M. Kennema, P. C. A. Bruijnincx and B. M. Weckhuysen,

View Article Online
DOI: 10.1039/D5SE00645G

Angew. Chemie - Int. Ed., 2016, **55**, 8164–8215.
51 C. M. Hansen, *Hansen Solubility Parameters*, Taylor & Francis Group, Second Edi., 2007.
52 X. Tan, Q. Zhang, W. Wang, X. Zhuang, Y. Deng and Z. Yuan, *Fuel*, 2019, **249**, 334–340.
53 Q. Li, Y. Dong, K. D. Hammond and C. Wan, *J. Mol. Liq.*, 2021, **344**, 117779.
54 E. Jasiukaitytė-Grojzdek, M. Huš, M. Grilc and B. Likozar, *ACS Sustain. Chem. Eng.*, 2020, **8**, 17475–17486.
55 Y. H. Xu, P. Zeng, M. F. Li, J. Bian and F. Peng, *Sep. Purif. Technol.*, 2021, **279**, 119780.
56 I. Cybulska, G. Brudecki, K. Rosentrater, J. L. Julson and H. Lei, *Bioresour. Technol.*, 2012, **118**, 30–36.
57 X. Erdocia, R. Prado, M. Á. Corcuera and J. Labidi, *J. Ind. Eng. Chem.*, 2014, **20**, 1103–1108.
58 C. Inkrod, M. Raita, V. Champreda and N. Laosiripojana, *Bioenergy Res.*, 2018, **11**, 277–290.
59 H. Yang, R. Yan, H. Chen, D. H. Lee and C. Zheng, *Fuel*, 2007, **86**, 1781–1788.
60 D. Watkins, M. Nuruddin, M. Hosur, A. Tcherbi-Narteh and S. Jeelani, *J. Mater. Res. Technol.*, 2015, **4**, 26–32.
61 K. Wang, Y. Jin, S. Sun, Y. Huang, J. Peng, J. Luo, Q. Zhang, Y. Qiu, C. Fang and J. Han, *ACS Omega*, 2017, **2**, 1687–1695.
62 N. Zhang, Q. Liu, W. Chen, M. Wan, X. Li, L. Wang, L. Xue and W. Zhang, *J. Power Sources*, 2018, **378**, 331–337.
63 F. Wang, T. Zhang and F. Ran, *Electrochim. Acta*, 2023, **441**, 141770.
64 V. Augustyn, J. Come, M. A. Lowe, J. W. Kim, P. L. Taberna, S. H. Tolbert, H. D. Abruña, P. Simon and B. Dunn, *Nat. Mater.*, 2013, **12**, 518–522.
65 Y. Liu, H. Dai, L. Wu, W. Zhou, L. He, W. Wang, W. Yan, Q. Huang, L. Fu and Y. Wu, *Adv. Energy Mater.*, 2019, **9**, 1–9.
66 Y. Wan, Y. Liu, D. Chao, W. Li and D. Zhao, *Nano Mater. Sci.*, 2022, **5**, 189–201.
67 C. Chen, Y. Huang, Y. Zhu, Z. Zhang, Z. Guang, Z. Meng and P. Liu, *ACS Sustain. Chem. Eng.*, 2020, **8**, 1497–1506.
68 W. Li, X. Guo, K. Song, J. Chen, J. Zhang, G. Tang, C. Liu, W. Chen and C. Shen, *Adv. Energy Mater.*, 2023, **13**, 1–10.
69 L. Minnetti, F. M. Maddar, A. K. Haridas, M. Capener, F. Nobili and I. Hasa, *Batter. Supercaps*, 2025, **8**, e202400645.
70 H. Darjazi, L. Bottoni, H. R. Moazami, S. J. Rezvani, L. Balducci and L. Sbrascini, *Mater. Today Sustain.*, 2023, 100313.
71 H. Chen, M. Ling, L. Hencz, H. Y. Ling, G. Li, Z. Lin, G. Liu and S. Zhang, *Chem. Rev.*, 2018, **118**, 8936–8982.
72 A. Staffolani, L. Sbrascini, L. Bottoni, L. Minnetti, H. Darjazi, A. Trapananti and F. Paparoni, *Energy Adv.*, , DOI:10.1039/d4ya00335g.
73 L. Minnetti, L. Sbrascini, A. Staffolani, V. Marangon, F. Nobili and J. Hassoun, *J. Energy Chem.*, 2024, **96**, 300–317.

View Article Online
DOI: 10.1039/D5SE00645G

Data Availability Statement

All the produced data are available within this manuscript.

View Article Online
DOI: 10.1039/D5SE00645G

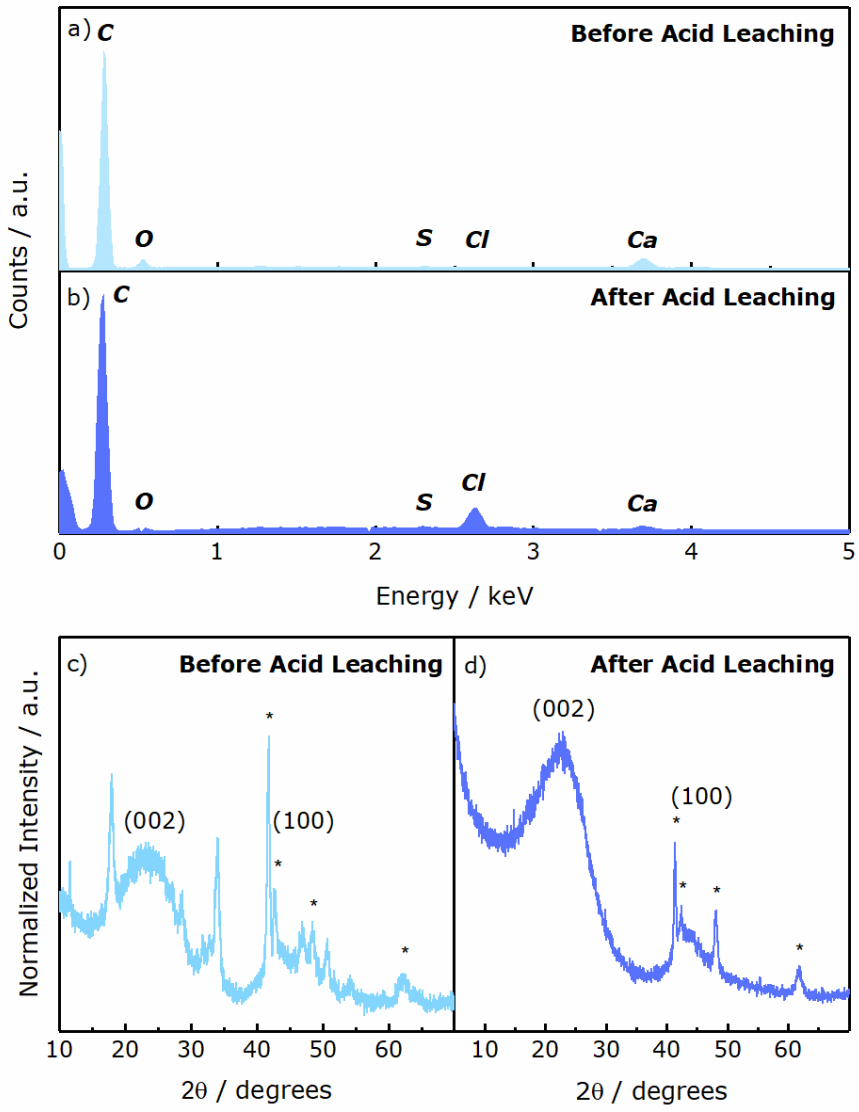

89x106mm (300 x 300 DPI)

View Article Online
DOI: 10.1039/D5SE00645G

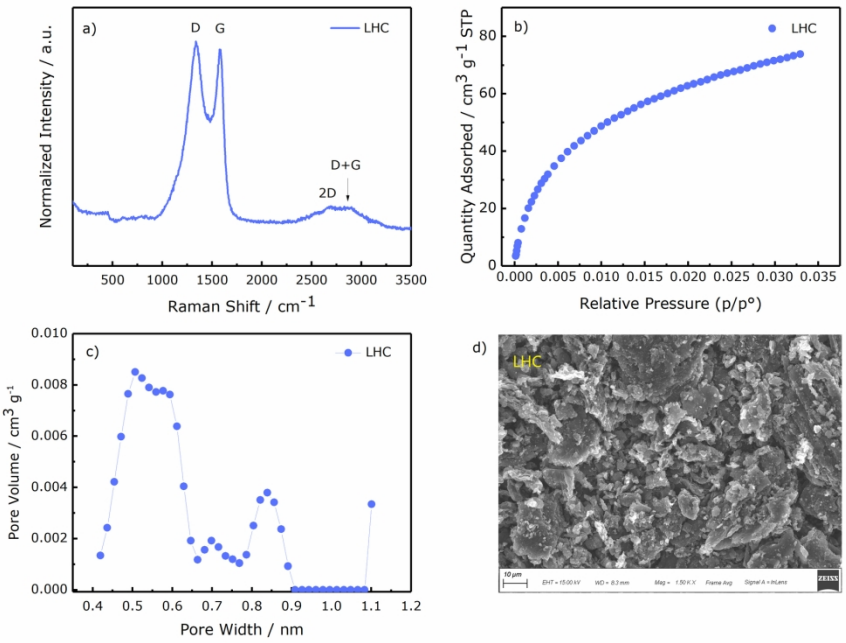

179x125mm (300 x 300 DPI)

View Article Online
DOI: 10.1039/D5SE00645G

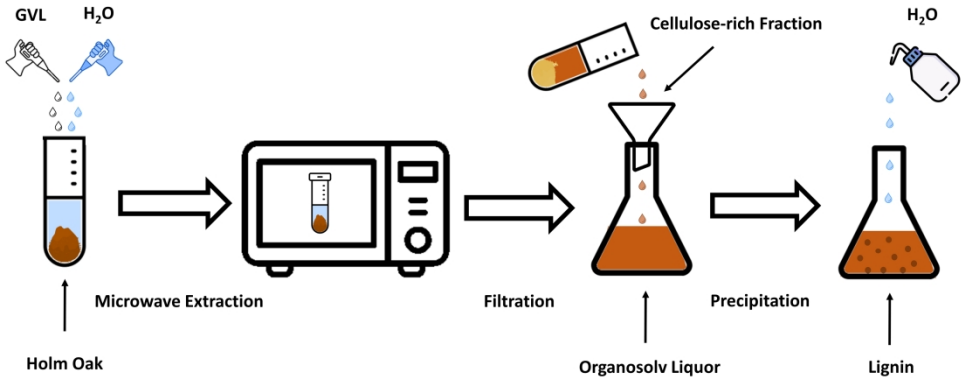

338x190mm (300 x 300 DPI)

View Article Online
DOI: 10.1039/D5SE00645G

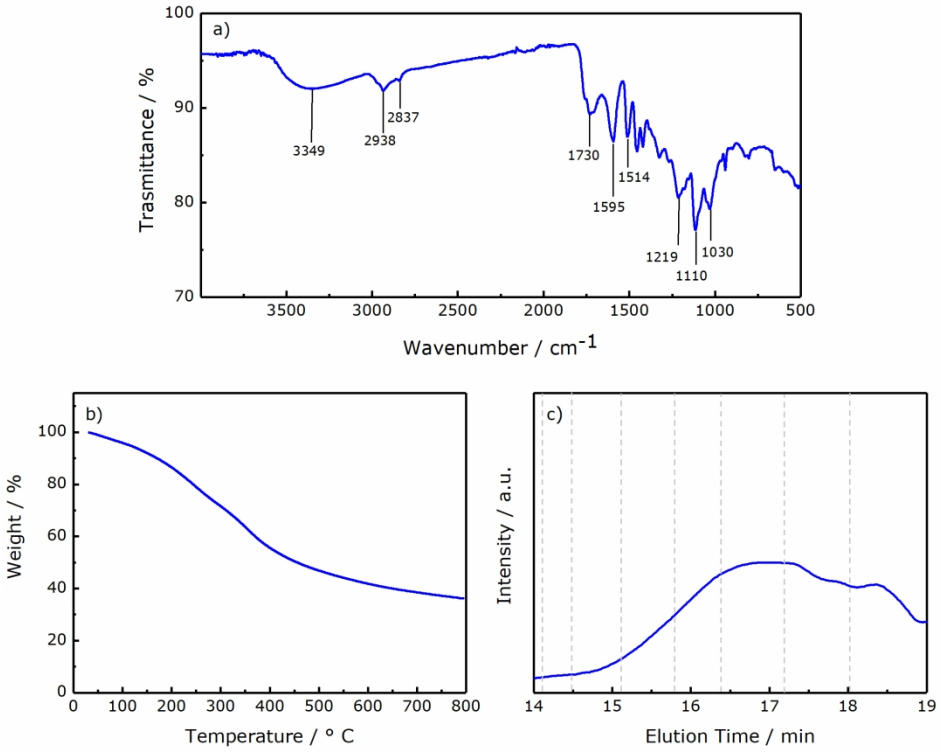

189x159mm (300 x 300 DPI)

View Article Online
DOI: 10.1039/D5SE00645G

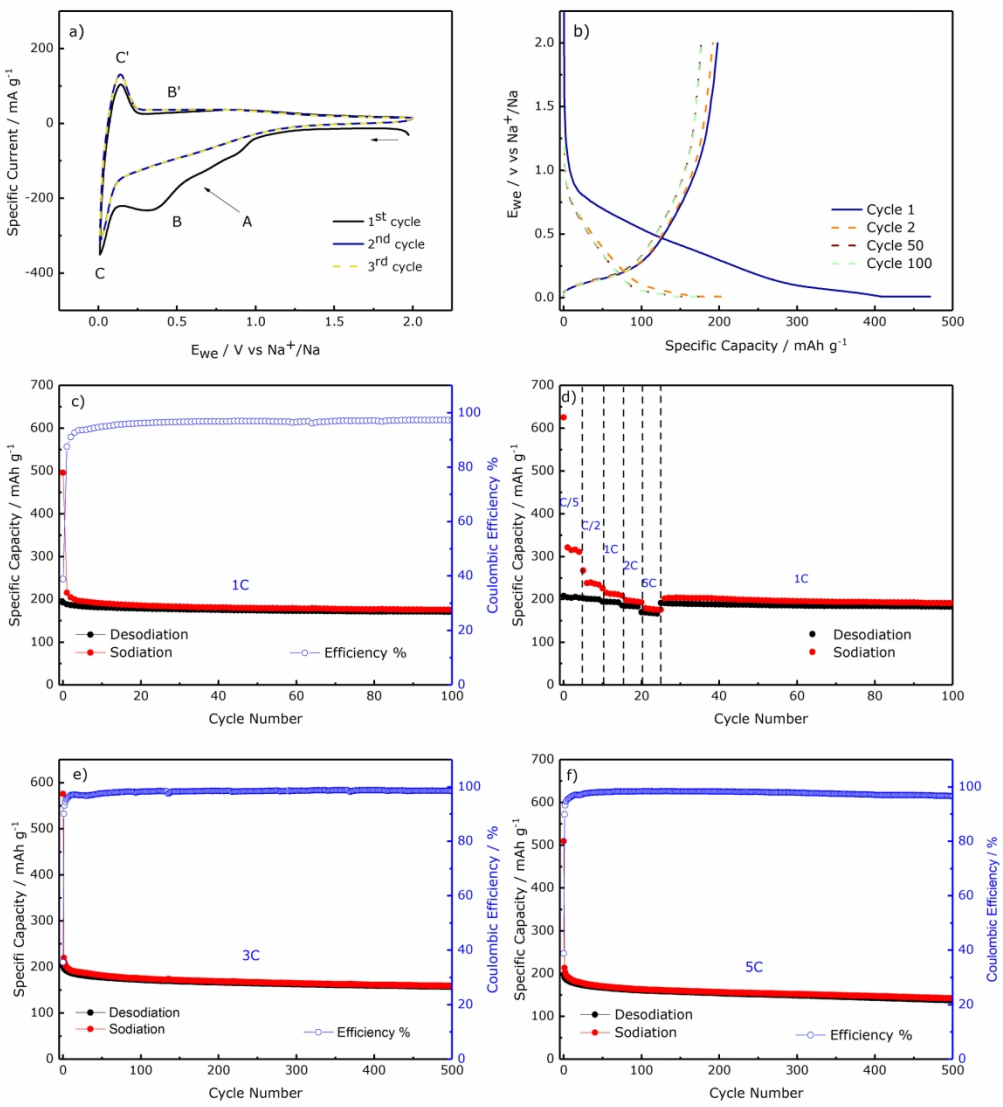

189x212mm (300 x 300 DPI)

View Article Online
DOI: 10.1039/D5SE00645G

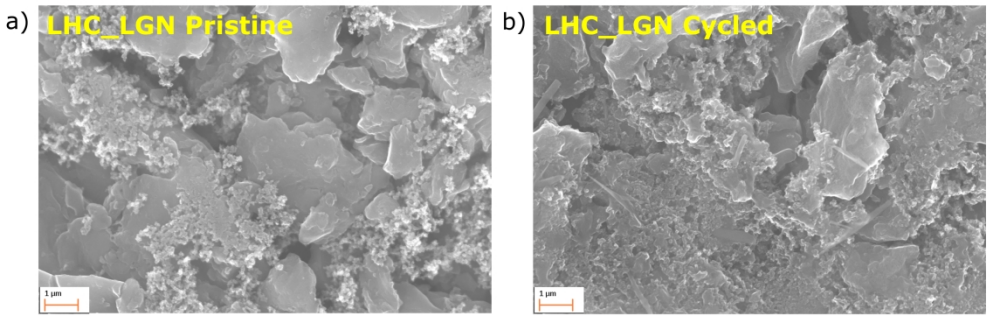

338x190mm (300 x 300 DPI)

View Article Online
DOI: 10.1039/D5SE00645G

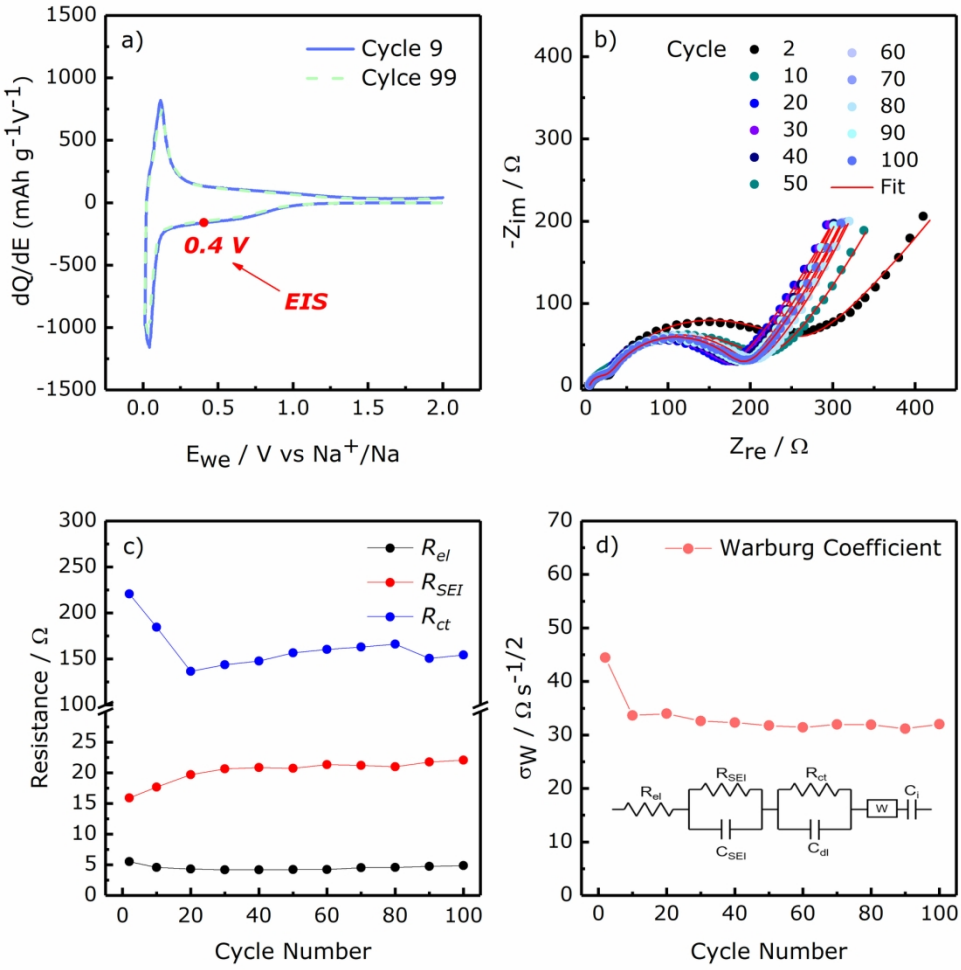

160x169mm (300 x 300 DPI)